Pergamon

0956-7151(94)00286-X

Acta metall. mater. Vol. 43, No. 2, pp. 603–620, 1995

0956-7151/95 $9.50 + 0.00

COMPACTION OF AN ARRAY OF SPHERICAL PARTICLES

N. OGBONNA and N. A. FLECK†

Department of Engineering, Cambridge University, Trumpington Street, Cambridge CB2 1PZ, England

(Received 6 May 1994)

Abstract—The compaction response has been investigated for an array of spherical particles composed of elastic, perfectly plastic material. Numerical simulations have been used to examine the evolution of contact size, contact pressure and macroscopic yield surface with the degree of compaction. It is found that the macroscopic yield surface of a compact has a corner at the loading point, and its shape evolves with increasing strain in a non self-similar fashion.

1. INTRODUCTION

A dominant mechanism of the densification of powders bonded by isolated contacts is the mutual plastic indentation of powder particles. The contact points between particles expand into contact areas as plastic deformation is induced by the applied macroscopic pressure. Particle deformation by contact growth prevails until porosity, which is interconnected initially, closes off. The compaction process then passes into a second stage where the compact behaves as a solid containing isolated pores.

Macroscopic constitutive laws for the plastic yielding of spherical powders, based on the process of contact growth between particles, have been developed for compaction under a purely hydrostatic stress state [1] and a non-hydrostatic stress state [2]. In these studies, the pressure at an interparticle contact was taken to be the slip-line solution for localized plastic deformation at the neck between two particles. Helle and co-workers [1] used Prandtl's solution for indentation of an infinite solid by a flat punch while Fleck and co-workers [2] used the solution given by Green [3] for the plastic yielding of a metal junction under combined shear and pressure. With increasing compaction, the plastic zone emanating from a contact begins to interact with the free surface of the particle and with the deformation zones of neighbouring contacts. The influence of such interaction on the compaction response of spherical powder has not so far been examined. In view of the technical use of compacted (and sintered) metal powders, it is of interest to investigate the effects of particle geometry and contact–contact interaction on the compaction response.

The yield behaviour of a powder aggregate bonded by isolated contacts remains unclear. Most of the existing yield laws have been obtained by a pragmatic empirical approach which consists of adding a pressure term to the yield function for a fully dense solid, and determining the unknown parameters from uniaxial compression tests (e.g. [4]) or from combined torsion and compression tests (e.g. [5]). This approach gives yield surfaces which are elliptical in shape. By constructing a micromechanical theory of compaction from the deformation behaviour of individual powder particles, Fleck *et al.* [2] found that a corner exists on the yield surface for spherical powders subjected to axisymmetric loading. Recent results of compaction experiments on powders with different morphologies [6, 7] indicate that the yield behaviour of a powder compact depends not only on the density of the compact, but also on the compaction strain path.

In this paper, we investigate the compaction behaviour of a regular array of spherical particles subjected to axisymmetrical loading. First, we examine the evolution of contact size and assess the influence of particle geometry on contact pressure, using the simple case of uniaxial compression of a line of spheres without a radial constraint. Second, we investigate the macroscopic stress–strain response for a simple cubic array of spheres subjected to the deformation states of (i) closed die and (ii) isostatic compaction. The shape of the yield surface is determined at various stages of deformation history.

2. POWDER STRUCTURE AND UNIT CELL

The arrangement of powder for this study is shown in Fig. 1(a). It consists of a simple cubic array of identical spheres, with the spheres initially touching each other at six contact points. The loading condition is axisymmetric.

The compaction response of the array of spheres will be discussed in terms of a representative unit cell of the aggregate. The unit cell is taken to consist of

†To whom all correspondence should be addressed.

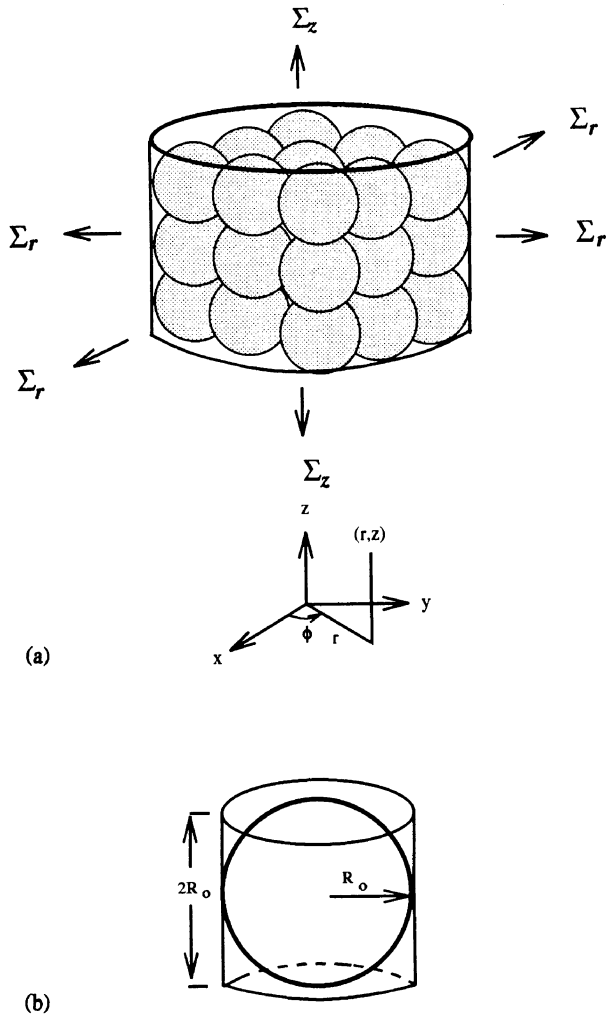

Fig. 1. Arrangement of powder and unit cell. (a) A simple cubic array of spheres subjected to an axisymmetric stress state (Σ_r, Σ_z). (b) The representative unit cell consisting of a single sphere circumscribed by a circular cylinder.

a single spherical particle circumscribed by a circular cylinder of radius R_o equal to that of the undeformed sphere, and height $2R_o$, as shown in Fig. 1(b). The relative density Δ is defined as the volume of solid material in the unit cell divided by the volume of the unit cell. Thus, the initial relative density $\Delta_o = 2/3$. This value is very close to 0.64 which is generally accepted as the initial relative density for a random dense packing of spheres.

Axisymmetric compaction of a simple cubic array of spheres leads to the development of four discrete contacts around the mid-section of each particle, in addition to a contact at the top and bottom of the particle. This 3D deformation state is simplified to axisymmetric deformation of each particle in the following manner. During compaction, the top and bottom planes of the unit cell surrounding a representative particle approach each other, and the circular cylindrical boundary of the cell shrinks in diameter. The deformed state of the particle is illustrated in Fig. 2. The contact surface normal to the axis of symmetry (axial contact) is a circle of radius a; an annular contact (radial contact) of width $2b$ and radius R is formed around the mid-section of the particle. The annular contact arises by virtue of the simplifying assumption of an axisymmetric distribution of contact between particles, and of axisymmetric deformation. It can be interpreted as the contribution from the four particle contacts surrounding the mid-section of a typical particle. The deformed cylindrical cell boundary has radius R and height $2H$.

By conservation of mass, we equate the volume of the deformed particle to the volume of the undeformed sphere of radius R_o and, thus, obtain the current relative density Δ as

$$\Delta = \frac{2}{3}\frac{R_o^3}{R^2 H}. \tag{1}$$

The local deformation of a typical particle is characterized by the radial and axial contact size parameters b and a, respectively, and the corresponding average contact pressures $\bar{p}_r$ and $\bar{p}_z$ defined by

$$\bar{p}_r = \frac{L_r}{4\pi R b}, \tag{2}$$

$$\bar{p}_z = \frac{L_z}{\pi a^2}. \tag{3}$$

Here, L_r is the radial load on the annular radial contact of width $2b$ and L_z is the axial load on the circular axial contact of radius a.

The macroscopic response of the aggregate is given by the average state of stress and strain in the representative unit cell. The logarithmic radial strain E_r and logarithmic axial strain E_z are related to the characteristic dimensions R and H of the deformed unit cell by

$$E_r = \ln\left(\frac{R}{R_o}\right), \tag{4}$$

$$E_z = \ln\left(\frac{H}{R_o}\right). \tag{5}$$

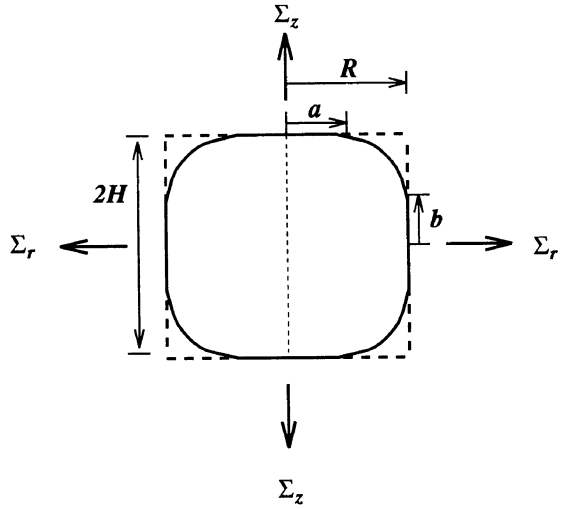

Fig. 2. Deformed state of the unit cell for a cubic array of spheres, showing characteristic dimensions and macroscopic stresses.

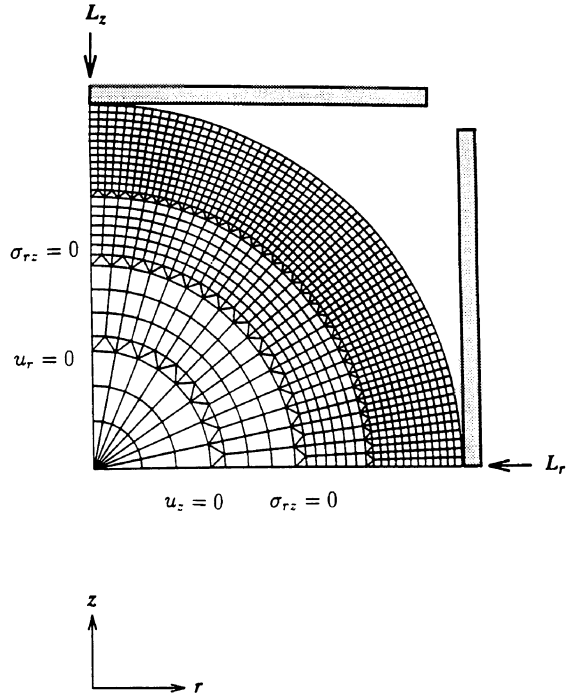

Fig. 3. Finite element mesh showing boundary and loading conditions.

The radial macroscopic stress Σ_r and axial macroscopic stress Σ_z on the walls of the unit cell are

$$\Sigma_r = \frac{b}{H}\bar{p}_r, \tag{6}$$

$$\Sigma_z = \frac{a^2}{R^2}\bar{p}_z. \tag{7}$$

For closed die compaction (i.e. uniaxial straining), E_r vanishes; for uniaxial compression with no radial constraint, Σ_r vanishes. In the latter case, the mechanical state of a particle is the same as for a sphere compressed between two flat frictionless plates.

3. FINITE ELEMENT ANALYSIS

The problem is to determine, at each stage of the compaction process, the macroscopic strain state (E_r, E_z) and the macroscopic stress state (Σ_r, Σ_z) for a cubic array of identical spheres subjected to axisymmetric loading. If we know the characteristic dimensions R and H of a deformed particle, the contact size parameters a and b, and the contact pressures $\bar{p}_r$ and $\bar{p}_z$, the macroscopic quantities can be calculated using equations (4)–(7). The task, therefore, is to solve the local problem of contact deformation.

We use numerical simulations to track the evolution of the contact area and the corresponding variation of contact pressure. This procedure is adopted for the purpose of obtaining accurate results which may then be used to appraise the accuracy of existing approximate analytic solutions. The ABAQUS† finite element (FE) method is used for the numerical simulations, and full account is taken of both finite strains and finite deformations.

Symmetry considerations indicate that it is necessary to analyse only the portion of the circular cylinder defined by the quadrant $(0 \leqslant r \leqslant R_o,\ 0 \leqslant z \leqslant R_o)$, where R_o is the radius of the undeformed sphere and (r, z) are cylindrical coordinates. The finite element mesh is shown in Fig. 3. It consists of 1024 quadratic and 176 triangular axisymmetric elements. The triangular elements are used mainly for the purpose of mesh grading in order to concentrate fine elements at the contact regions where a strong variation of field quantities is expected. All elements are of the hybrid type, with independent interpolation schemes for the displacement and pressure variables to permit the modelling of incompressible behaviour.

By virtue of axisymmetry, the displacements, strains and stresses are functions of only the cylindrical coordinates (r, z). Within an element, the displacement field is assumed to vary linearly so that the stress is constant. The boundary conditions are indicated in Fig. 3: zero normal displacement ($u_z = 0$) and zero shear traction ($\sigma_{rz} = 0$) are prescribed along the bottom surface ($z = 0$). The curved surface of the particle is traction free, and the radial displacement vanishes ($u_r = 0$) along the axis of symmetry $r = 0$. In order to simulate axisymmetric compaction, normal displacements are imposed along the top and right-hand side of the representative unit cell. Frictionless interface elements are used to impose the boundary displacement field, and to endow the particles with zero cohesive strength. The representative spherical particle is assumed to be made from an elastic, perfectly plastic, J_2-flow theory solid, with a yield strain $\epsilon_0 = 10^{-3}$ and Poisson's ratio $\nu = 0.3$.

The radial and axial displacements of the boundary of the representative unit cell are applied incrementally, on account of the history dependence of the material response. Both proportional and non-proportional straining paths are used to generate data for the yield behaviour of the unit cell. The proportional straining paths include the special cases of closed die compaction ($E_r = 0$) and isostatic compaction ($E_r = E_z$). The nonproportional paths are for uniaxial compression ($\Sigma_r = 0$) and for radial compression ($\Sigma_z = 0$). In order to probe the yield surface of the array of spheres, the unit cell is deformed to a prescribed relative density, unloaded to zero macroscopic stress, and then re-loaded to yield along different strain paths.

4. RESULTS AND DISCUSSION

The deformation of a representative spherical particle under uniaxial loading provides insight into the nature of contact growth and material flow, without the complexity introduced by a radial constraint. We shall discuss this case first, and then proceed to consider the deformation of a particle subjected to combined radial and axial constraints.

†ABAQUS, HKS Inc., Rhode Island, U.S.A.

4.1. Uniaxial compression

The representative spherical particle is compressed at its top and bottom, with vanishing radial stress. The deformed shape of the particle is characterized by the contract radius a, particle height $2H$ and particle diameter $2R$ at the mid-section.

4.1.1. Deformed particle geometry. Figure 4(a) shows the evolution of the geometric parameters a/R_o, H/R_o and R/R_o with the logarithmic axial

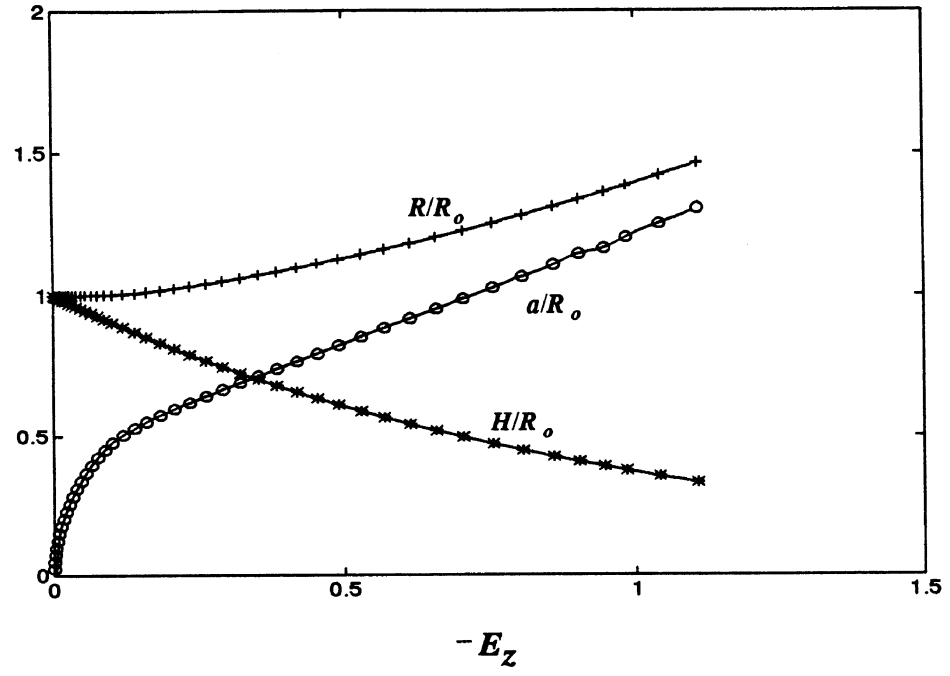

(a)

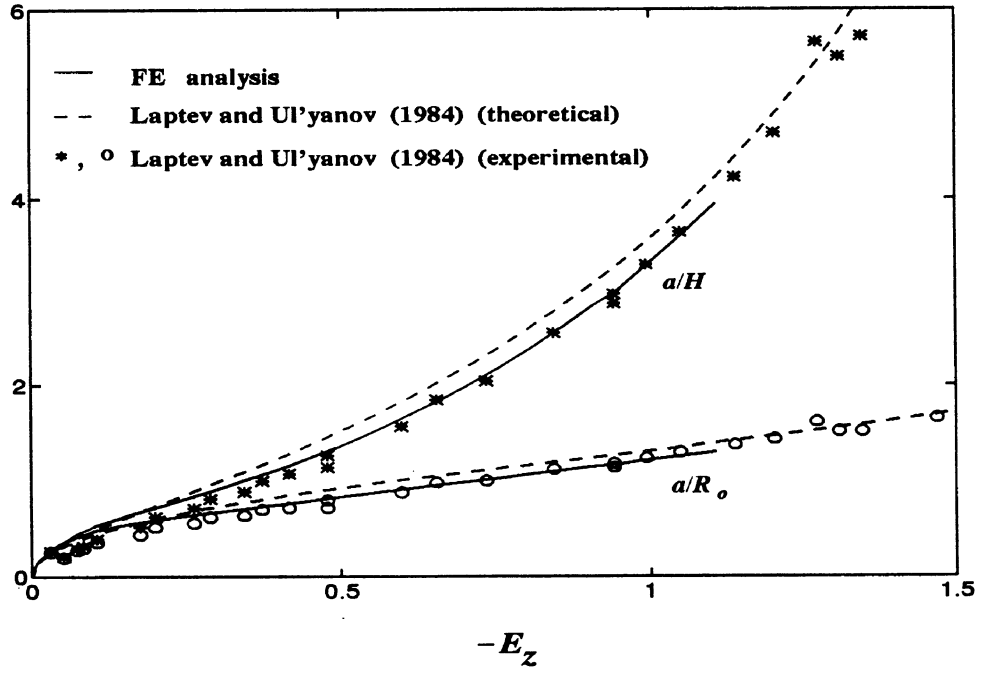

(b)

Fig. 4. (a) Evolution of contact radius a, half particle height H and particle mid-section radius R with increasing axial strain E_z for spherical particle under uniaxial compression with no radial constraint. (b) Comparison of finite element results for the contact radius with the theoretical and experimental results of Laptev and Ulyanov [8]. In both figures R_o is the radius of the undeformed particle.

strain $E_z = \ln(H/R_o)$. The normalized radius R/R_o of the mid-section is approximately constant ($R/R_o \approx 1$) for $-E_z < 0.1$; thereafter, it increases nonlinearly with axial strain. The lag between the start of plastic deformation at the mid-section of the particle and the start of plastic deformation at a contact offers some explanation for the calculated variation of the contact radius. During the initial period of contact deformation, plastic flow is localized near a contact; material displaced from the contact region remains in the vicinity of the contact and provides for rapid neck growth. With increasing deformation, plastic flow becomes non-localized and the rate of growth of the contact radius decreases. As plastic flow spreads over the full height of the particle, the mode of deformation changes to one where the lateral surface of the particle steadily moves outwards; consequently, R/R_o increases steadily.

Laptev and Ulyanov [8] have found an approximate analytical expression for the contact radius by assuming that the free surface of the particle maintains a spherical shape during deformation. The contact radius a is then related to half the particle height H according to

$$\frac{a}{R_o} = \left[\frac{2}{3}\left(\frac{H}{R_o}\right)^{-1}\left(1-\left(\frac{H}{R_o}\right)^3\right)\right]^{1/2} \qquad (8)$$

where R_o is the radius of the undeformed sphere. Laptev and Ulyanov [8] have also presented experimental data for uniaxial compression of lead spheres. Their experimental results, and their theoretical solution [given by equation (8)], are compared with the calculated results in Fig. 4(b). The figure shows (i) the normalized contact radius a/R_o, and (ii) the ratio a/H of contact radius to half the particle height, as functions of the logarithmic axial strain E_z. The finite element results show better agreement with the experimental data than the analytical solution of Laptev and Ulyanov. The lack of quantitative agreement between their solution and the calculated results is attributed to their assumption of uniform radial expansion of the free surface of the deforming sphere. The present analysis shows that, for logarithmic axial strains of magnitude greater than 25%, this assumption leads to an overprediction of the contact radius for a given particle height.

The evolution of particle shape is shown in Fig. 5(a) for the case of uniaxial compression. It is evident that the material initially accumulates at the edge of contact with negligible change in diameter of the mid-section of the particle. Contours of effective plastic strain $\bar{\epsilon}$ are given in Fig. 5(b) during the initial stage of localized plasticity close to the contact; $\bar{\epsilon}$ is defined as $\bar{\epsilon} = \sqrt{(\frac{2}{3})\epsilon_{ij}^p \epsilon_{ij}^p}$, where ϵ_{ij}^p is the plastic strain. With increasing degree of compaction, the plastic zone spreads throughout the particle and the mid-section bulges.

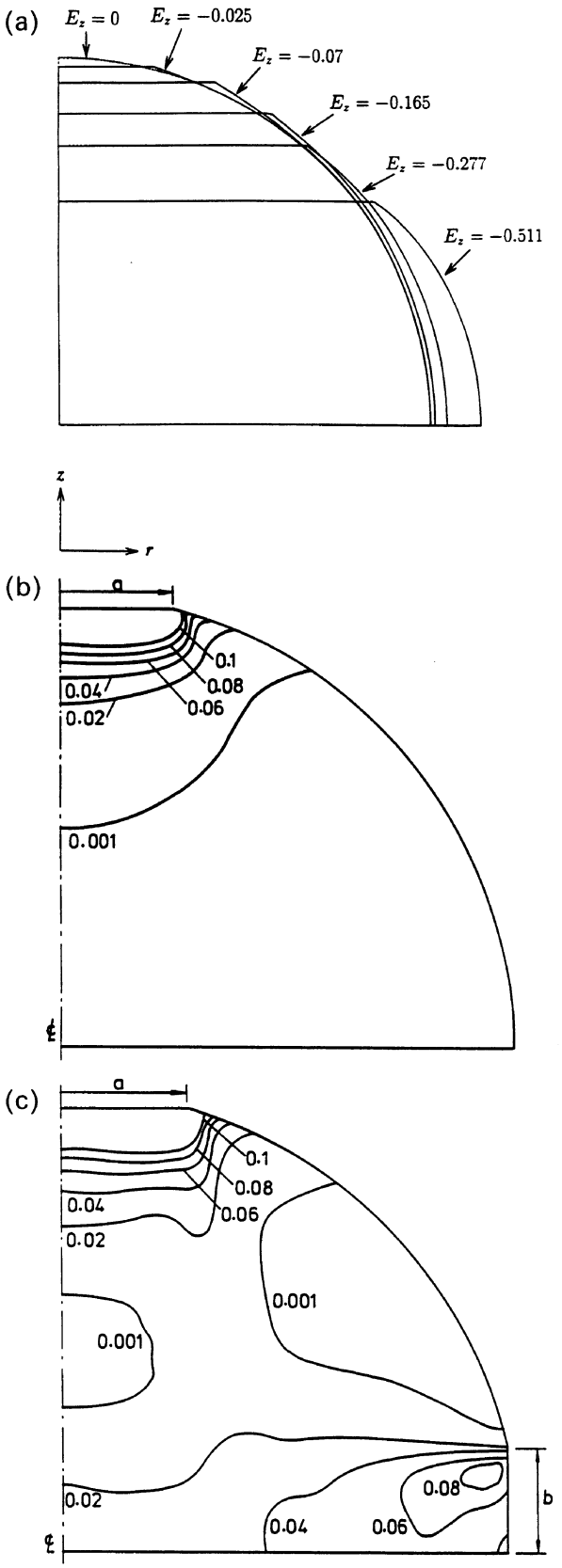

Fig. 5. (a) Shape change of a spherical particle under uniaxial compression. (b) Effective plastic strain distribution for uniaxial compression, $E_z = -0.025$. (c) Effective plastic strain distribution for isostatic compression, $E_z = -0.025$.

4.1.2. Contact pressure and macroscopic stress. Figure 6(a) shows the variation of the normalized mean contact pressure $\bar{p}_z/\sigma_y$ with logarithmic axial strain $E_z = \ln(H/R_o)$. The initial high values of the contact pressure are due to numerical inaccuracies associated with small contact sizes in relation to

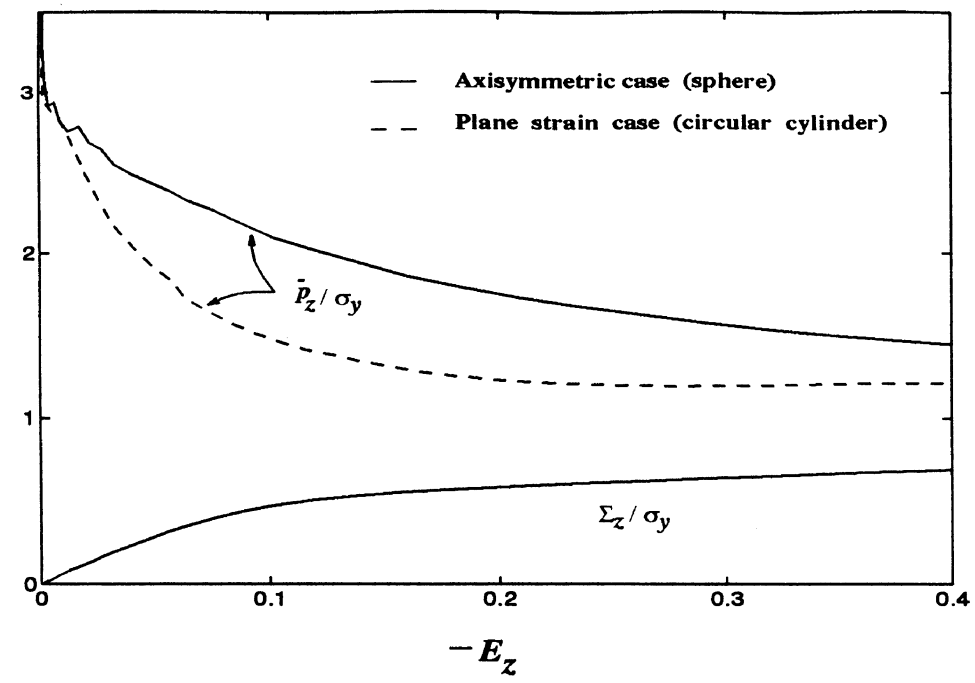

(a)

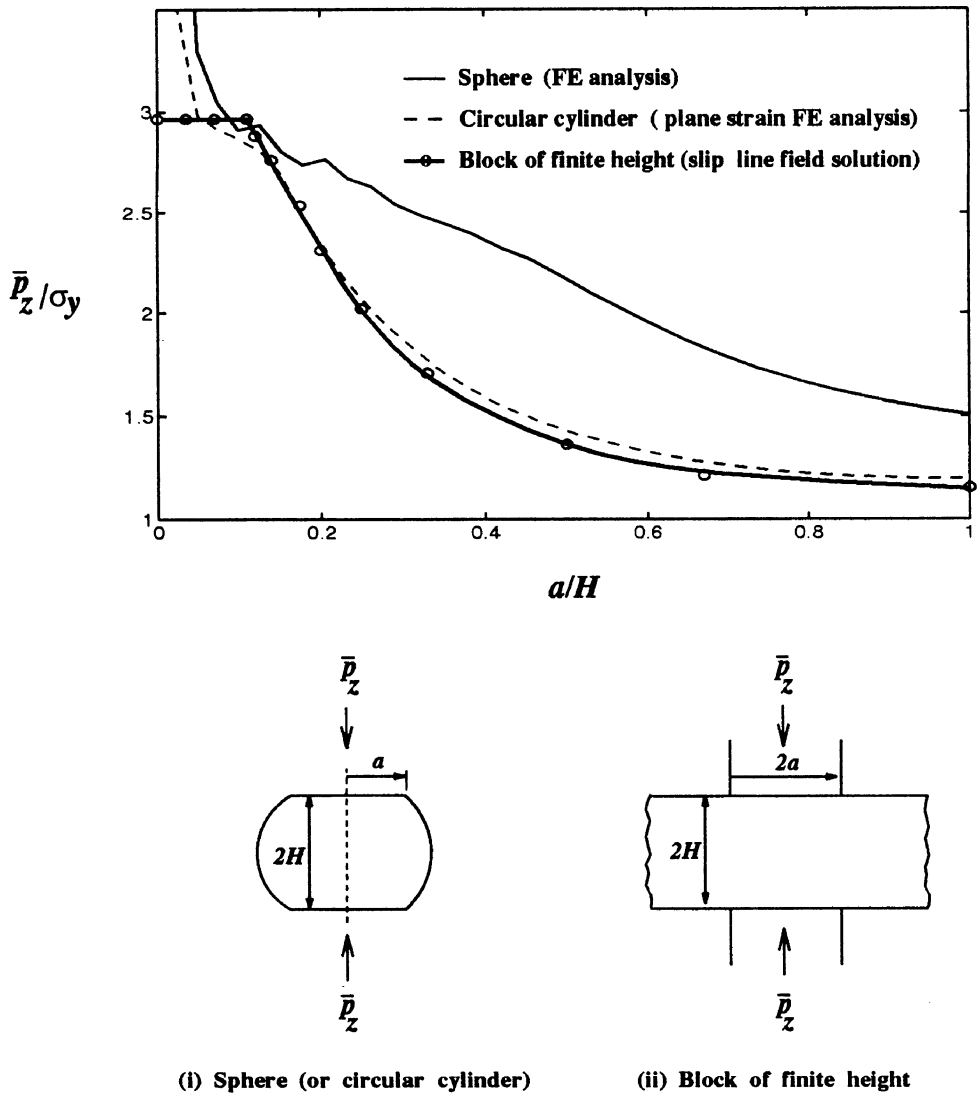

(b)

Fig. 6. (a) Contact pressure $\bar{p}_z$ and macroscopic stress Σ_z for uniaxial compression of a particle with no radial constraint. (b) Finite element results for a sphere are compared with the finite element result for a cylinder and the slip line field solution for an infinitely wide rectangular block. Stresses are normalized by the uniaxial yield stress σ_y of the material.

element size. For $-E_z > 0.003$, where the solution is accurate, $\bar{p}_z/\sigma_y$ falls continuously from a value of about 3. The decrease in contact pressure is attributed to the effects of particle geometry and interaction of the opposite contacts. The variation of the normalized macroscopic stress Σ_z/σ_y with logarithmic axial strain E_z is included in Fig. 6(a). In contrast to the contact pressure, the macroscopic stress increases from zero towards the yield stress σ_y of the material.

For comparison, we have calculated by the finite element method the average contact pressure for plane strain deformation of a circular cylinder of initial radius R_o compressed between two frictionless plates. The mesh and material properties are identical to that for the axisymmetric problem. The variation of the average contact pressure for the plane strain case is qualitatively similar to that for the axisymmetric case, as shown in Fig. 6(a). However, the initial fall in contact pressure with increasing axial strain is more rapid for plane strain deformation than for axisymmetric deformation. The plane strain contact pressure settles to almost the plane strain yield strength, $\bar{p}_z/\sigma_y = 2/\sqrt{3}$, at about $-E_z = 0.3$. In the axisymmetric case, much larger axial strains are required for the contact pressure to settle to the limiting value of the uniaxial yield strength.

In Fig. 6(b), the calculated average contact pressure for both plane strain and axisymmetric deformation are compared with the slip line field solution for compression of an infinitely wide block of finite height $2H$ made from a rigid, perfectly plastic solid (see for example [9]). Here, $\bar{p}_z/\sigma_y$ is plotted against the ratio a/H, where H is half the height of the compressed solid (which may be a sphere, a circular cylinder or a block). The slip line field solution for the block of finite height is constant initially, with $\bar{p}_z/\sigma_y \approx 3$. It begins to fall at about $a/H = 0.12$ due to interaction of plastic fields between the opposite contacts. We note that the calculated plane strain results and the slip line field solution are in good agreement.

4.2. *Isostatic compression*

We consider the limiting case of the representative unit cell subjected to isostatic straining. The variation of the macroscopic mean stress $\Sigma_m = (2\Sigma_r + \Sigma_z)/3$ with increasing relative density Δ is shown in Fig. 7. The mean stress varies nonlinearly with the relative density.

A relation given by Helle *et al.* [1] for the hydrostatic compaction of a random dense packing of equal spheres is

$$P_y = 3\Delta^2\left(\frac{\Delta - \Delta_o}{1 - \Delta_o}\right)\sigma_y, \quad (\Delta_o \leqslant \Delta \leqslant 0.9) \qquad (9)$$

where P_y is the macroscopic pressure to cause yield, σ_y is the uniaxial yield stress of the material composing the spheres, Δ_o and Δ are the initial and current relative densities of the compact. A plot of equation (9) is included in Fig. 7 for comparison. For $\Delta < 0.75$,

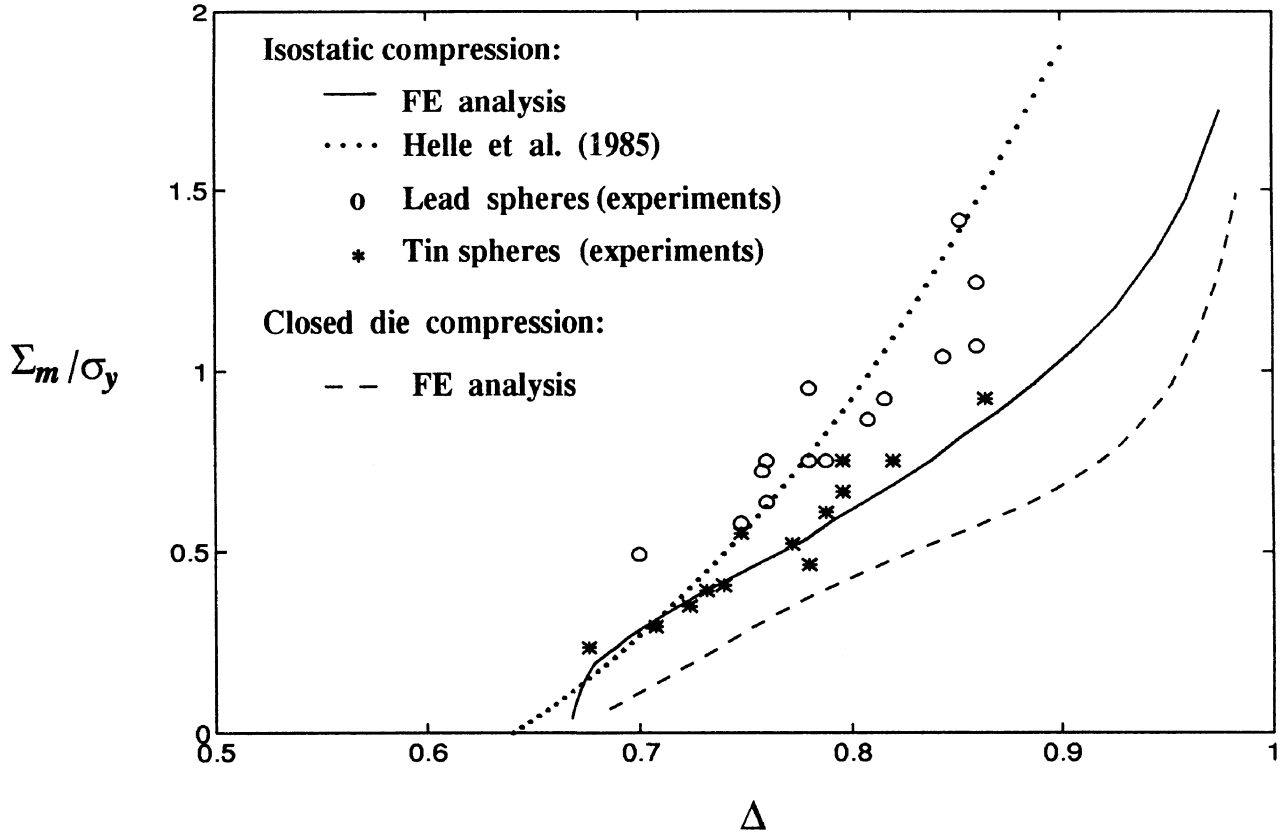

Fig. 7. Macroscopic mean stress Σ_m as a function of the relative density Δ. The experimental data are from Laptev and Podlesnyi [10].

the relation (9) is in reasonable agreement with the calculated results for isostatic compression; for $\Delta > 0.75$; it predicts significantly higher mean stress than the present analysis. We note that in deriving equation (9), Helle and co-workers [1] assumed that the contact pressure at each stage of deformation is given by the slip line field solution for indentation of a half-space by a flat punch. Thus, their result does not include the effects of particle geometry and contact–contact interaction. On the other hand, the finite element results incorporate both effects. We also mention that Helle and co-workers considered (correctly) a purely hydrostatic stress state, while the stress state in the current analysis is not purely hydrostatic, although the strain state is isostatic. This peculiar feature arises due to the assumption of an axisymmetric distribution of contacts around each particle, and of axisymmetric deformation. It is, therefore, not surprising that the result of the present analysis does not coincide precisely with the predictions of Helle *et al.* [1].

Laptev and Podlesnyi [10] have provided experimental data for the hydrostatic compaction of lead and tin powders. The finite element results show good agreement with their data for tin, and poor agreement with their data for lead. Equation (9) shows better agreement with the data for lead, than for tin. The predicted macroscopic mean stress for closed die compression is included in Fig. 7. It is observed that the mean stress to achieve a given density is higher for isostatic compression than for closed die compression. In contrast, the constitutive law given by Fleck *et al.* [2] predicts the same pressure vs relative density response for closed die compaction and isostatic compaction.

The plastic strain distribution for isostatic compression is displayed in Fig. 5(c) for $E_z = -0.025$. Although plasticity is concentrated in the region of the contacts (both at the top of the particle and at the mid-plane), the plastic zones have begun to overlap between the contacts. For the case of uniaxial compression with $E_z = -0.025$ [see Fig. 5(b)], plastic deformation is local to the contact at the top of the particle.

4.2.1. Contact area. It is of interest to examine the development of contact areas A_r and A_z normal to the radial and axial directions, respectively. We consider the cases of isostatic compression ($\dot{E}_z = \dot{E}_r$) and closed die compression ($\dot{E}_r = 0$). These two cases relate directly to practical situations where powders are processed by isostatic and closed die pressing.

The growth of the contact areas A_r and A_z with increasing relative density Δ is shown in Fig. 8(a) for both isostatic and closed die compression of the representative unit cell. The contact areas have been normalized by the total surface area of an undeformed particle $A_o = 4\pi R_o^2$, where R_o is the radius of the undeformed particle.

For isostatic compression, the normalized axial contact area A_z/A_o varies approximately linearly with relative density, while the variation of the normalized radial contact A_r/A_o is nonlinear. A_r/A_o exceeds A_z/A_o throughout the densification process. This is not surprising since the radial contact corresponds to an annular ring and mimics the contribution from four particles at the mid-section of a typical particle in a simple cubic array of spheres.

For closed die compression (i.e. uniaxial straining), the radial contact area A_r is less than the axial contact area A_z for $\Delta < 0.8$; thereafter, A_r exceeds A_z. The fact that $A_r < A_z$ initially is to be expected since the mid-section of the particle (which represents the initial point of radial contact) starts to deform only when plastic flow has spread through the entire particle thickness. We note further from Fig. 8(a) that isostatic compression gives a higher radial contact area, and a lower axial contact area, than closed die compression at a given relative density.

Next, consider the overall contact area of a particle, rather than the details of contact growth in a particular direction. For this purpose, we define a specific contact area A_s as the total contact surface area per particle A_{total} divided by the total surface area of the undeformed particle $A_o = 4\pi R_o^2$. The variation of the specific contact area A_s with relative density Δ is shown in Fig. 8(b) for both isostatic and closed die compression. We note that the total contact area per particle is larger for isostatic compression than for closed die compression. In the case of closed die compression, the computed variation of A_s is reasonably linear in Δ for $\Delta_o \leqslant \Delta \leqslant 0.85$, where Δ_o is the initial relative density.

For isostatic compaction of a random dense packing of identical spheres, Helle *et al.* [1] have proposed that the evolution of each contact area A_c with the relative density Δ can be described by the semi-empirical relation

$$A_c = \frac{\pi}{3}\left(\frac{\Delta - \Delta_o}{1 - \Delta_o}\right) R_o^2 \tag{10}$$

where Δ_o is the initial relative density and R_o is the initial radius of a particle. Helle and co-workers assumed that the coordination number (average number of contacts per particle) is

$$Z = 12\Delta \tag{11}$$

and so the specific contact area is

$$A_s = \Delta(\Delta - \Delta_o)/(1 - \Delta_o). \tag{12}$$

This expression, and the experimental data given by Fischmeister and Artz [11] for compaction of spherical bronze powder, are included in Fig. 8(b). In plotting their results, we have taken the initial relative density for a dense random packing of spheres to be $\Delta_o = 0.64$. The finite element results and the empirical relation of Helle *et al.* are in good agreement with the experimental data of Fischmeister and Artz [11]. The finite element analysis predicts a significantly larger specific contact area A_s for isostatic compression in comparison with closed die compression. This is not

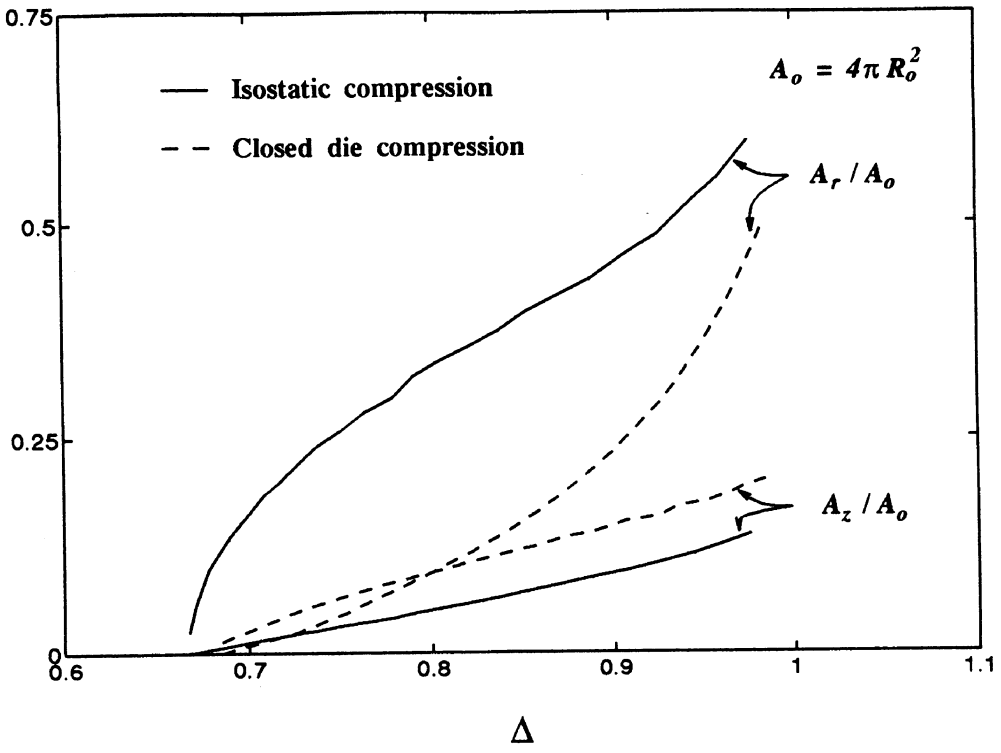

(a)

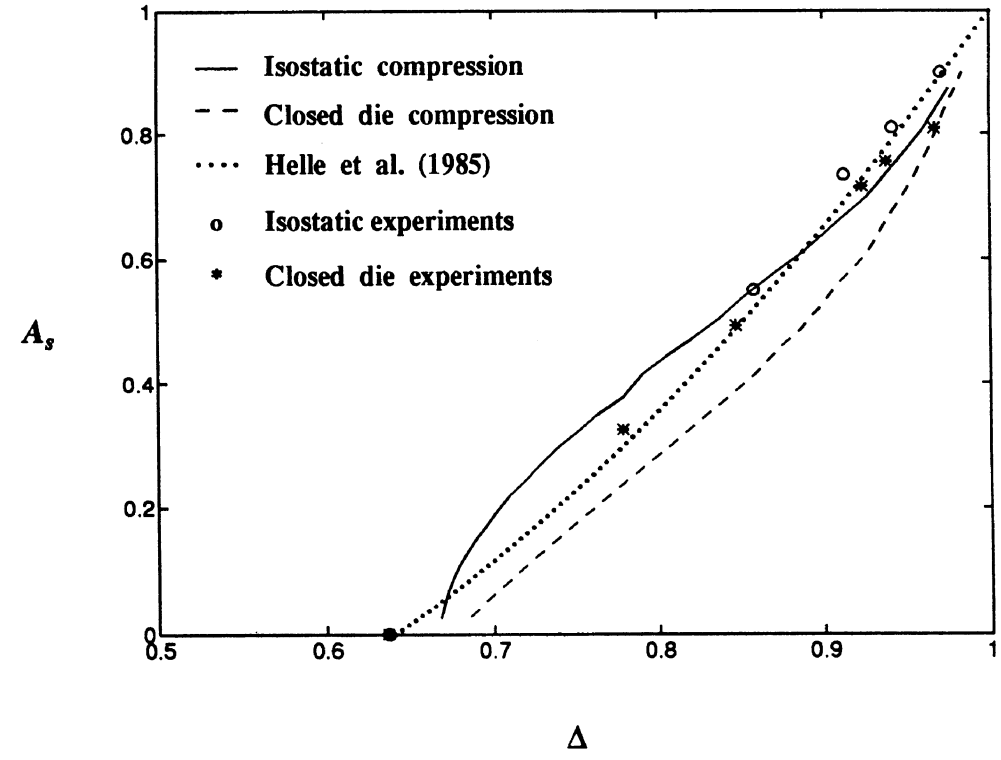

(b)

Fig. 8. Evolution of contact area with relative density Δ for isostatic, and closed die, compression of a spherical particle. (a) Normalized radial contact area A_r/A_o and normalized axial contact area A_z/A_o. (b) Specific contact area A_s $(=A_{total}/A_o)$. The experimental data are from Fischmeister and Artz [11].

reflected by the experimental data. At least part of the discrepancy is due to the fact that the finite element analysis assumes axisymmetric deformation at the local level for each particle. In reality, powder exists as a dense random packing and the deformation state for each particle is 3D.

4.3. Combined radial and axial compression

For the practical case of powder compaction, the powder particles deform under a multi-axial stress state. Here, we consider the case of axisymmetric stressing. Radial and axial constraints are imposed on the representative unit cell by prescribing strain rates $\dot{E}_r$ and $\dot{E}_z$ in the radial and axial directions, respectively, Proportional strain paths are described by

$$\dot{E}_z = \dot{E}_r \tan\psi, \quad (\pi \leqslant \psi \leqslant 3\pi/2)$$

where the phase angle ψ is a constant. The straining paths in strain space (E_r, E_z) are shown in Fig. 9. In this figure, we have included the strain paths observed for uniaxial compression ($\Sigma_r = 0$) and for radial compression ($\Sigma_z = 0$); these cases involve proportional stressing but slightly non-proportional straining.

4.3.1. Contact pressures and macroscopic stresses. The mean contact pressures $\bar{p}_r$ and $\bar{p}_z$ have been calculated using equations (2) and (3), respectively. A plot of the normalized axial mean contact pressure $\bar{p}_z/\sigma_y$ vs the magnitude of the logarithmic axial strain E_z is shown in Fig. 10(a) for a number of straining paths. Similar to the case of uniaxial compression [see Fig. 6(a)], the mean contact pressure falls initially. However, at some critical value of the axial strain, the mean contact pressure starts to increase. The geometric hardening response found for the case of combined radial and axial constraints is not surprising. Material displaced from the contact region is forced to extrude up through the continuously decreasing gap between neighbouring contacts. This increases the constraint on the deformation process and a higher driving pressure is then required. The minimum value of the mean contact pressure and the corresponding value of the axial strain vary with the straining path. In particular, for isostatic straining, the minimum value of $\bar{p}_z/\sigma_y$ is 1.92 and occurs at about 10% logarithmic axial strain while, for a closed die strain state ($\dot{E}_r = 0$), it is about 13% less and occurs at an axial strain of approx. 30%.

The macroscopic stresses Σ_r and Σ_z have been calculated using equations (6) and (7), respectively. The variation of the normalized macroscopic axial stress Σ_z/σ_y with increasing axial strain is shown in Fig. 10(b) for a number of straining paths. These stress–strain curves differ from the uniaxial compression curve [see Fig. 6(a)] by the exhibition of a continued hardening response.

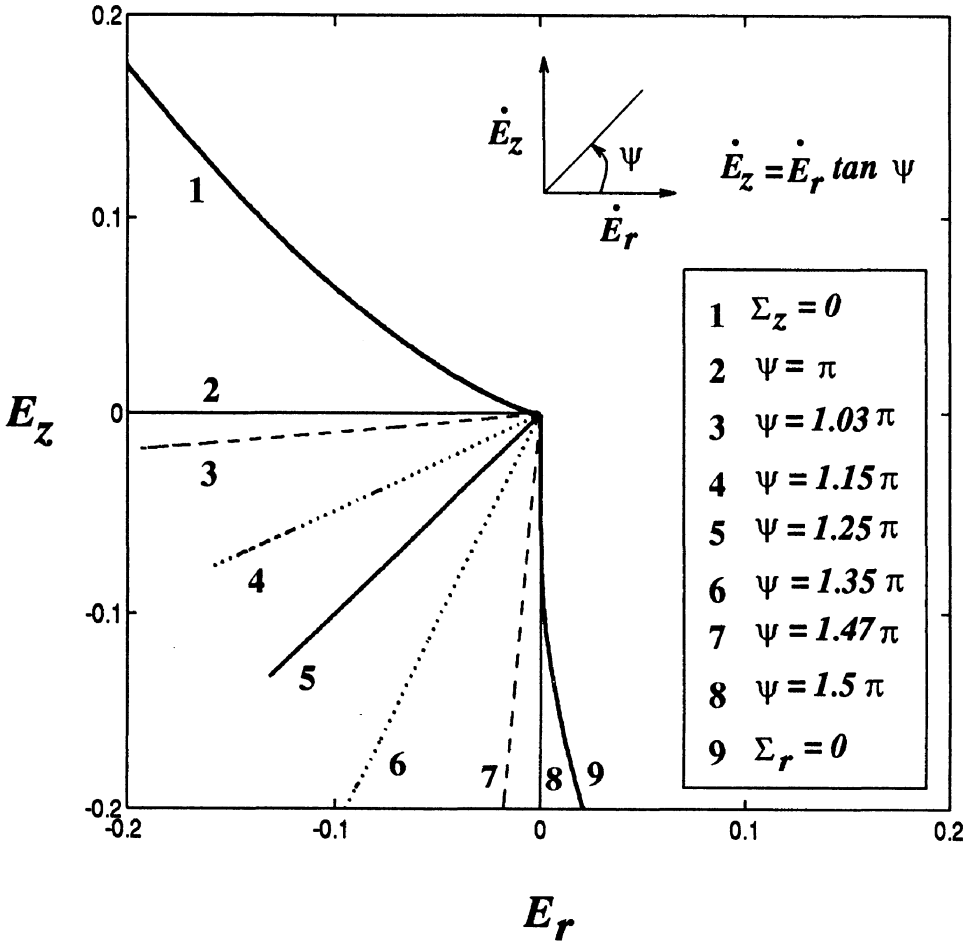

Fig. 9. Compaction strain paths.

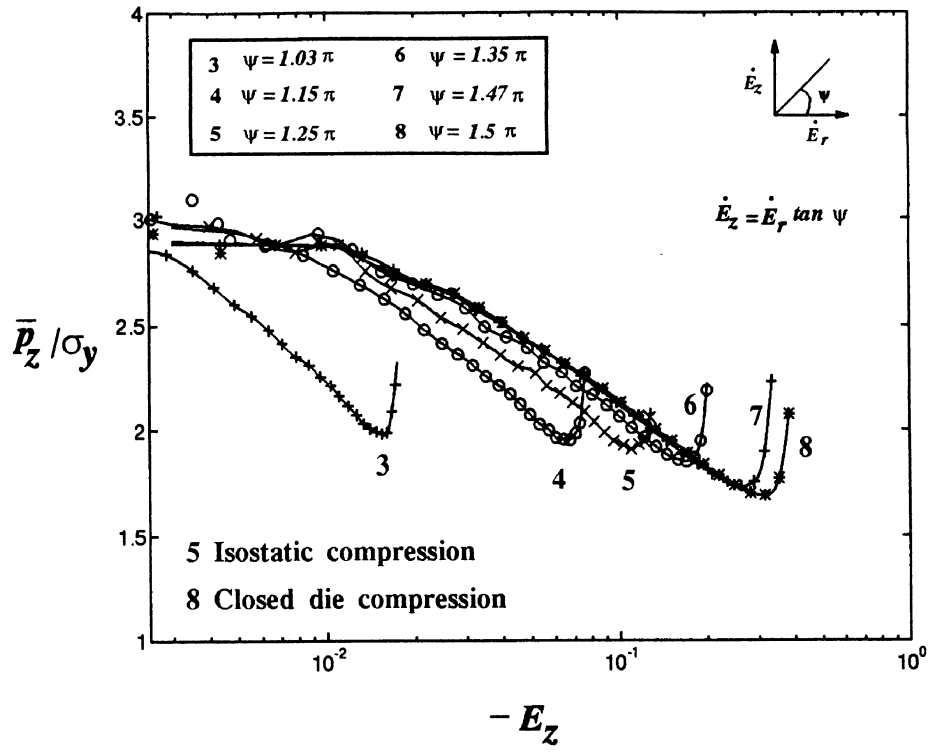

(a)

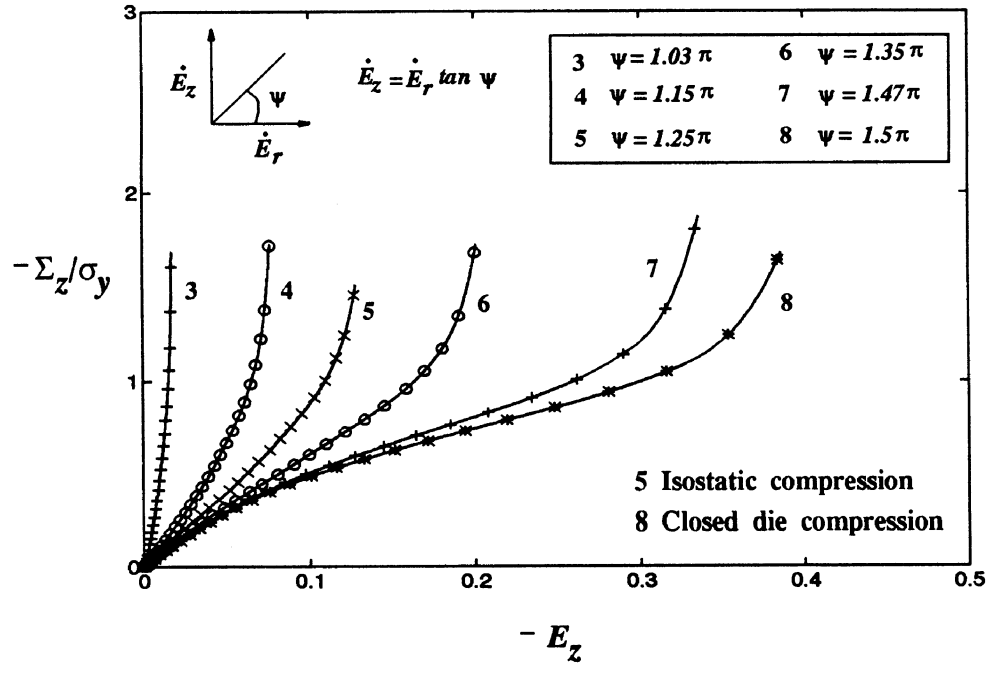

(b)

Fig. 10. Evolution of contact and macroscopic stresses with true axial strain for a spherical particle under combined radial and axial compression. (a) Normalized axial contact stress $\bar{p}_z/\sigma_y$. (b) Normalized macroscopic axial stress Σ_z/σ_y.

The normalized mean radial contact pressure $\bar{p}_r/\sigma_y$ is plotted against the magnitude of the logarithmic axial strain E_z in Fig. 11(a); and the variation of the normalized macroscopic radial stress Σ_r/σ_y with increasing axial strain is given in Fig. 11(b). The radial contact pressure and the macroscopic radial stress vary with the logarithmic axial strain E_z in a manner similar to that of the corresponding axial quantities.

4.3.2. Isodensity curves. Experimental difficulties have limited laboratory investigations of the yield behaviour of a powder compact to the generation of isodensity curves which do not involve probing the yield surface. The procedure consists of deforming a powder aggregate continuously along different stress paths, and evaluating the locus of stress states required to produce a compact of prescribed relative

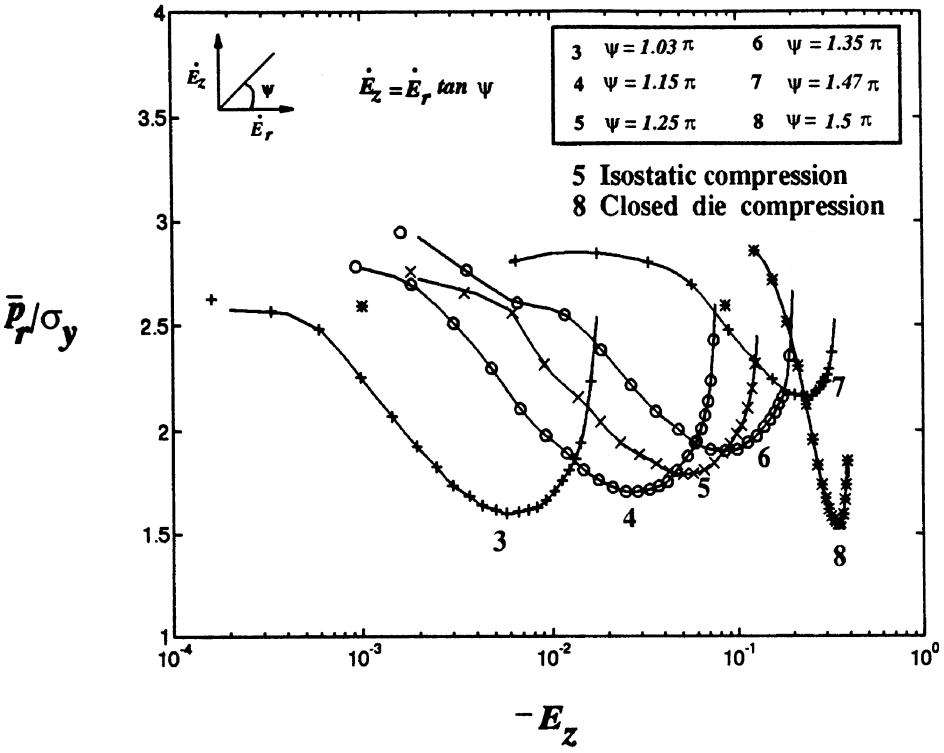

(a)

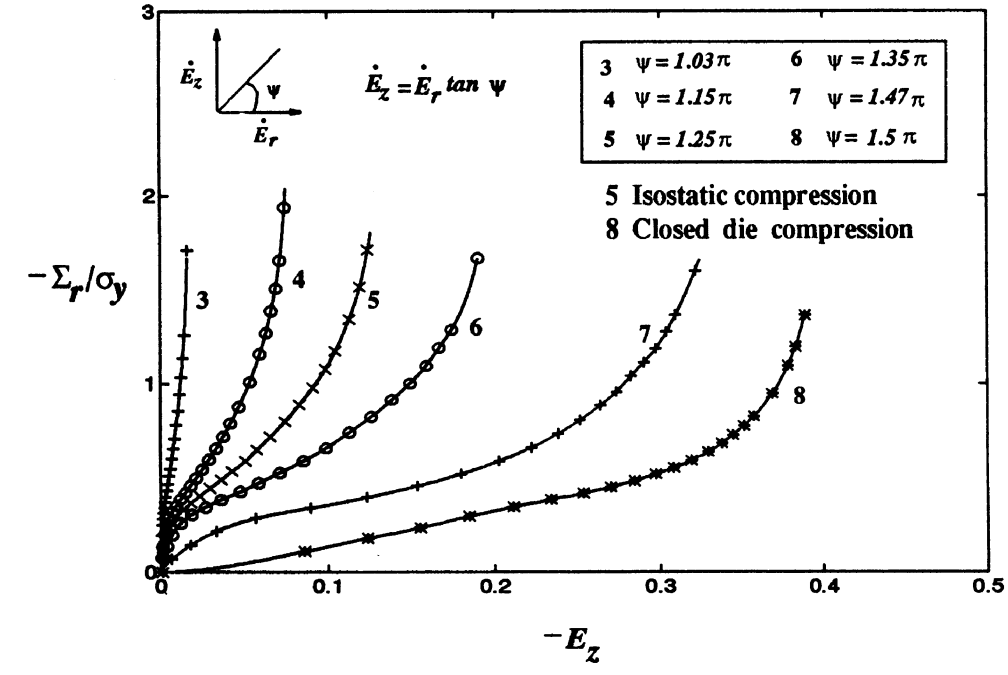

(b)

Fig. 11. Evolution of (a) normalized radial contact stress $\bar{p}_r/\sigma_y$ and (b) normalized macroscopic radial stress Σ_r/σ_y with true axial strain E_z.

density. This method has been used to study the yield behaviour of iron powder [6] and copper powder [7].

We have evaluated the isodensity curves for a simple cubic array of spherical particles deformed along the different loading paths shown in Fig. 9. A plot of the isodensity curves for $\Delta = 0.7$, 0.8 and 0.95 is shown in Fig. 12. The results are presented in Σ_m vs Σ space, where

$$\Sigma_m = (2\Sigma_r + \Sigma_z)/3 \tag{13}$$

is the macroscopic mean stress, and

$$\Sigma = \Sigma_z - \Sigma_r \tag{14}$$

is a measure of the macroscopic deviatoric stress. In the plot, we have normalized Σ_m and Σ by the uniaxial yield stress σ_y of the material composing the spherical particles. The isodensity curves are not symmetrical about the hydrostatic stress axis ($\Sigma_m = 0$); the curves also change shape as the relative density Δ increases from 0.7 to 0.95. The curve for $\Delta = 0.95$ has an apex in the neighbourhood of the loading point corresponding to an isostatic straining path. Nevertheless, the isodensity curves are smooth, with no corner development.

4.4. *The macroscopic yield surface*

The probing method has been used to determine the shape of the yield surface for a compact of given relative density. In this method, the representative unit cell of the simple cubic array of spherical particles is first strained to a prescribed relative density and unloaded to zero macroscopic stress. The compact that results from this operation (henceforth referred to as the "precompact") is then re-loaded along a prescribed straining path until it yields. This procedure is repeated for different straining paths. The locus of macroscopic stress at the point of plastic collapse gives the shape of the limit yield surface.

The yield surfaces for a precompact produced by isostatic straining (isostatic precompact) and one produced by closed die compression (closed die precompact) have been determined. The re-loading paths correspond to those shown in Fig. 9: the macroscopic strain rates $\dot{E}_r$ and $\dot{E}_z$ in the radial and axial directions, respectively, are related by $\dot{E}_z = \dot{E}_r \tan\psi$, where $\pi < \psi < 3\pi/2$. Typical stress–strain curves used to evaluate the yield point of a precompact during the re-loading process are shown in Fig. 13. In general, plastic collapse of a precompact occurs in an elastic, perfectly plastic manner. The macroscopic stress displays a plateau at a macroscopic strain of 6×10^{-4} to 2×10^{-3} as ψ varies from π to $3\pi/2$. For cases where the limiting yield stress is not clear, we have evaluated yield at 0.002 plastic strain.

Figure 14 shows the yield surfaces for an isostatic precompact and a closed die precompact of relative density $\Delta = 0.8$. In this plot, the macroscopic radial stress Σ_r and the macroscopic axial stress Σ_z have been normalized by the uniaxial yield stress σ_y of the solid. The direction of the macroscopic strain rate

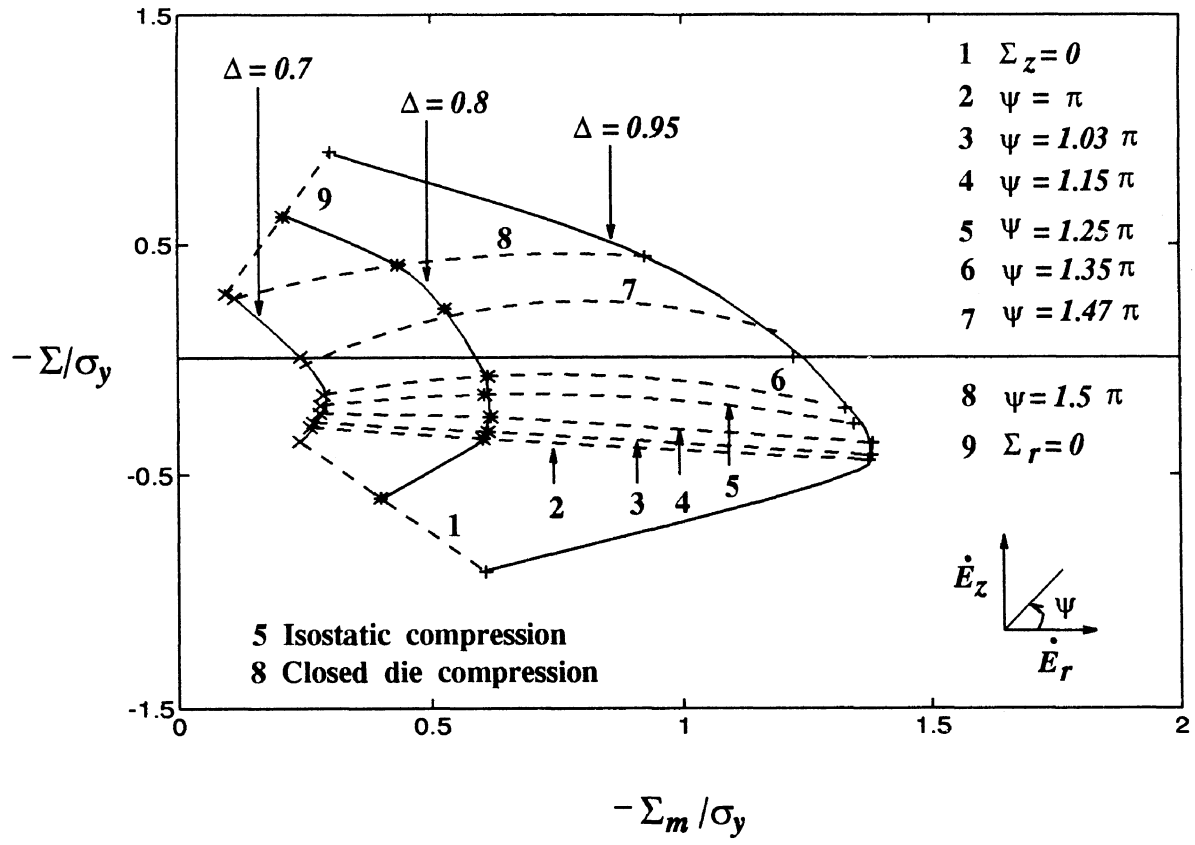

Fig. 12. Isodensity curves at relative density $\Delta = 0.7$, 0.8 and 0.95 in terms of macroscopic mean stress Σ_m and macroscopic deviatoric stress Σ.

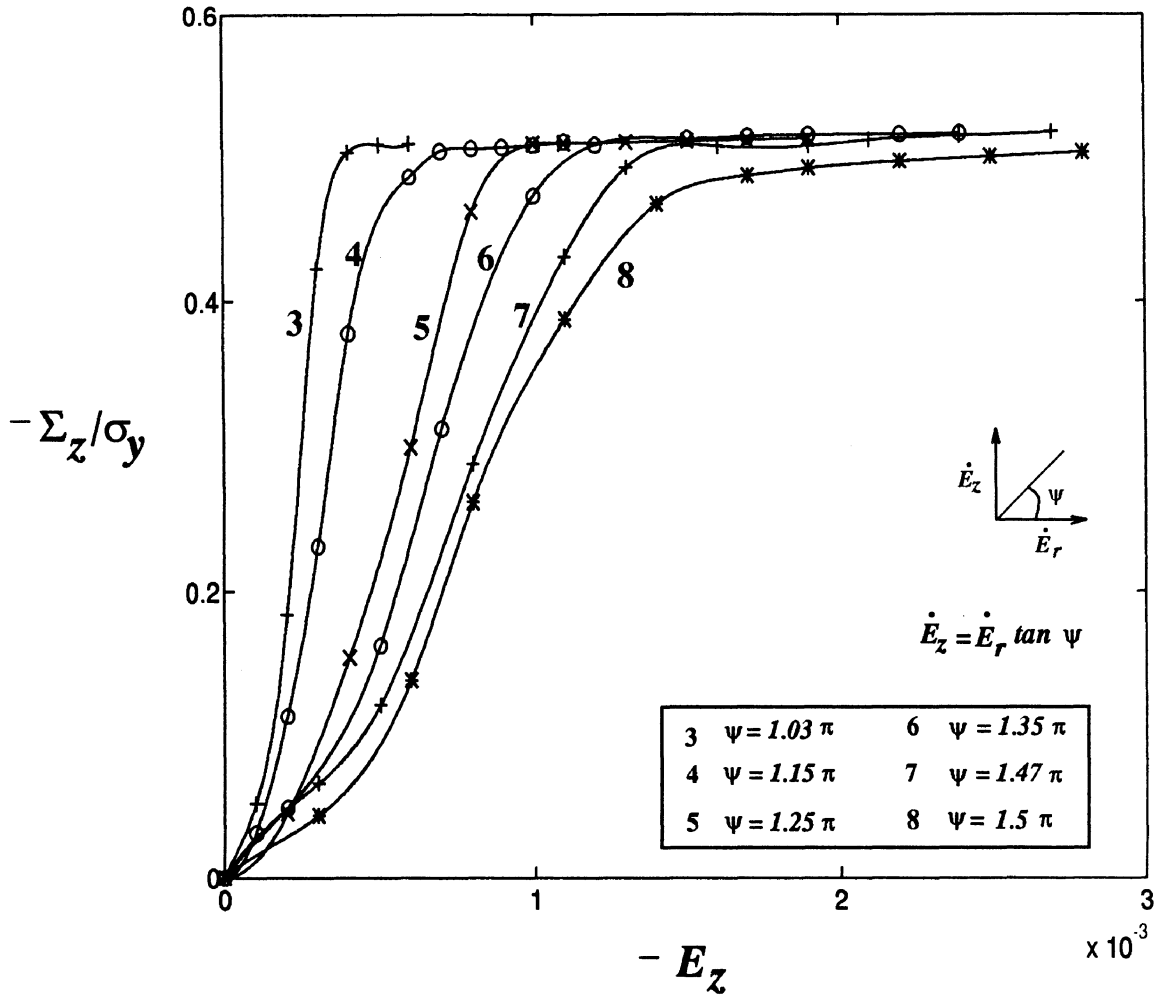

Fig. 13. Typical stress–strain curves used to evaluate the yield point of a precompact along various strain paths.

vector $(2\dot{E}_r, \dot{E}_z)$ is indicated at the loading points. In constructing the yield surfaces, the normality rule has been adopted so that the strain rate vector at each point is normal to the yield surface. Note that the lines $\Sigma_r = 0$ and $\Sigma_z = 0$ form part of the boundary for the yield surface. This is because the present analysis assumes cohesionless contact between the particles. Consequently, only compressive contact stresses are admissible; otherwise, contacts become disrupted and the compact returns to a loose, unadhered state.

For the isostatic precompact, a corner exists on the yield surface at the loading point which corresponds to an isostatic strain path. Similarly, the yield surface for a closed die precompact has a vertex at the loading point. The isostatic precompact has a lower yield stress in uniaxial compression and a higher yield stress in pure radial compression than the closed die precompact, in spite of the fact that both have the same relative density. This demonstrates that the yield behaviour of the aggregate of spheres is not just a function of the relative density; it also depends on the previous deformation path. Path dependence of the yield behaviour of compacted iron and copper powders has been observed experimentally by Gurson and McCabe [6] and Brown and Abou-Chedid [7]. The issue of path dependence of the yield behaviour of powders is important in practice as the strength of components fabricated by powder compaction may be influenced by the deformation paths used to reach the final shape.

It is of interest to examine how the shape of the yield surface evolves with relative density. As case studies, we consider the yield surfaces of an isostatic precompact and a closed die precompact at relative density $\Delta = 0.7$, 0.8 and 0.9. The calculated yield surfaces at these densities are shown in (Σ_r, Σ_z) space in Fig. 15(a), and in (Σ_m, Σ) space in Fig. 15(b). For both isostatic and closed die precompacts, the shape of the yield surface changes as the compaction process passes from Stage I densification ($\Delta = 0.7$) to moderate densification ($\Delta = 0.8$) and then to Stage II compaction ($\Delta = 0.95$). At all densities, a corner exists at the loading point corresponding to the initial compaction strain path (i.e. the loading path used to produce the precompact).

A yield surface proposed by Fleck *et al.* [2] for a random aggregate of rigid, perfectly plastic metal particles bonded by isolated contacts is

$$\phi(\Sigma_m, \Sigma, \Delta) = \left(\frac{\sqrt{5}\Sigma_m}{3P_y}\right)^2 + \left(\frac{5|\Sigma|}{18P_y} + \frac{2}{3}\right)^2 - 1 = 0, \quad (\Delta_o \leqslant \Delta \leqslant 0.9) \quad (15)$$

where P_y is the macroscopic stress to cause yield under a purely hydrostatic stress state. P_y is related to the relative density Δ by equation (9). Gurson [12] assumed that the pores in a particulate solid, rather than the interparticle contacts, are isolated; his expression for the yield surface of a porous solid is

$$\phi_G(\Sigma_m, \Sigma, \Delta) = \frac{2(1-\Delta)}{\Delta^2}\left[-1+\cosh\left(\frac{3\Sigma_m}{2\sigma_y}\right)\right] + \left(\frac{\Sigma}{\sigma_y \Delta}\right)^2 - 1 = 0. \quad (16)$$

These two yield surfaces are compared with the calculated results for an isostatic precompact in Fig. 16(a), and with the results for a closed die precompact in Fig. 16(b). In each case, the calculated yield surface lies partly outside that predicted by Fleck *et al.* [2] for $\Delta = 0.7$; and entirely within it for $\Delta > 0.7$. Both the yield surfaces obtained from the above finite element calculations and the yield surface given by Fleck *et al.* [2] have corners. However, the position of the corner is at the point of pure pressure for the model of Fleck and co-workers, while it is at the loading point corresponding to the initial compaction strain path in the present analysis. For both precompacts, the calculated yield surface at each density lies entirely within that predicted by Gurson [12]. Gurson's yield surfaces are elliptical in shape, with no corner development.

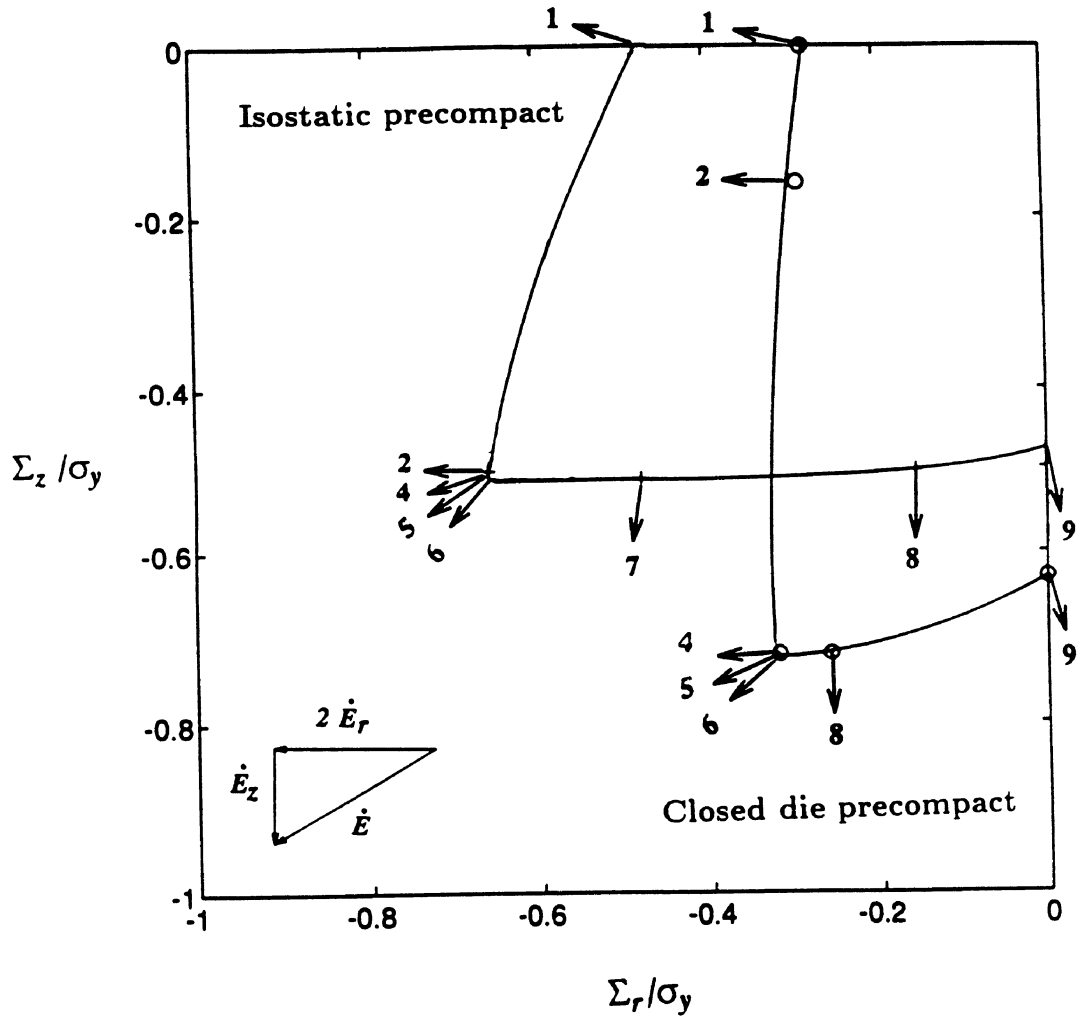

1	$\Sigma_z = 0$	4	$\psi = 1.15\pi$	7	$\psi = 1.47\pi$
2	$\psi = \pi$	5	$\psi = 1.25\pi$	8	$\psi = 1.5\pi$
3	$\psi = 1.03\pi$	6	$\psi = 1.35\pi$	9	$\Sigma_r = 0$

$\dot{E}_z = \dot{E}_r \tan\psi$

Fig. 14. Yield surfaces for precompacts of relative density $\Delta = 0.8$, showing the direction of the strain rate vector at a loading point.

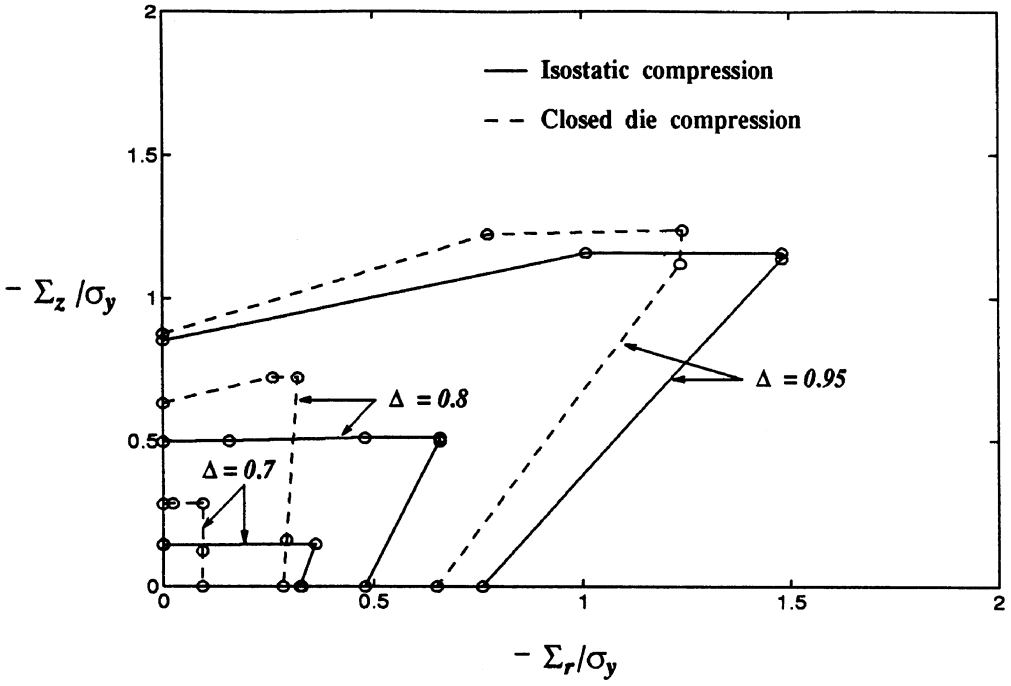

(a)

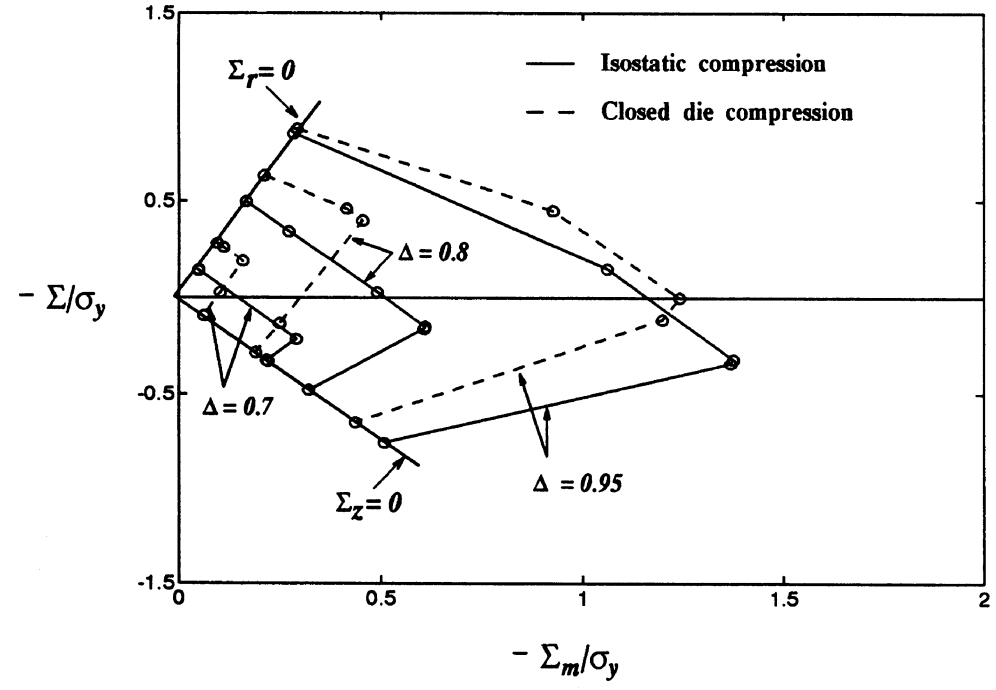

(b)

Fig. 15. Yield surfaces for isostatic and closed die precompacts at relative density $\Delta = 0.7$, 0.8 and 0.95. (a) Yield surface in terms of macroscopic radial stress Σ_r and macroscopic axial stress Σ_z. (b) Yield surface in terms of macroscopic mean stress Σ_m and macroscopic deviatoric stress Σ.

5. CONCLUDING REMARKS

A finite element investigation has been conducted of the compaction behaviour of an array of equal spherical particles. We have examined the evolution of contact size, the variation of the local stress at an interparticle contact, and the macroscopic yield behaviour of the aggregate.

Under uniaxial axisymmetric compression, the average contact stress decreases monotonically with increasing axial strain from a value of about $3\sigma_y$ to a value of σ_y. Under combined radial and axial

compression, the mean contact pressure initially decreases from about $3\sigma_y$. A stage is then reached where the contact pressure increases again in order to extrude material through the gap between particle contacts.

The finite element calculations suggest that a corner exists on the macroscopic yield surface at the loading point. Further studies are required in order to explore the practical significance of the corner.

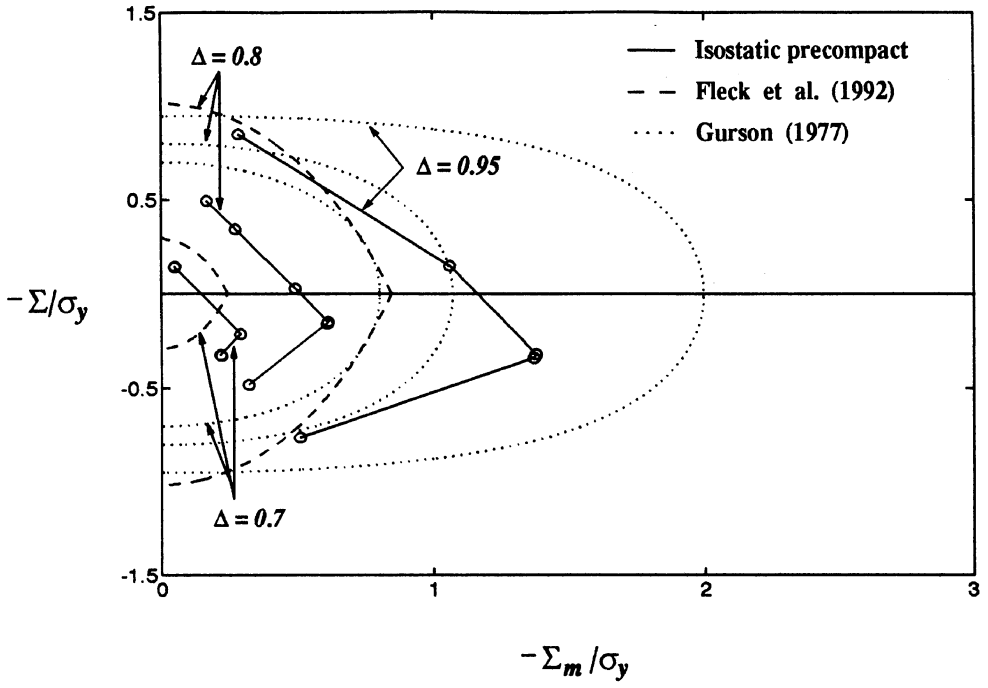

(a)

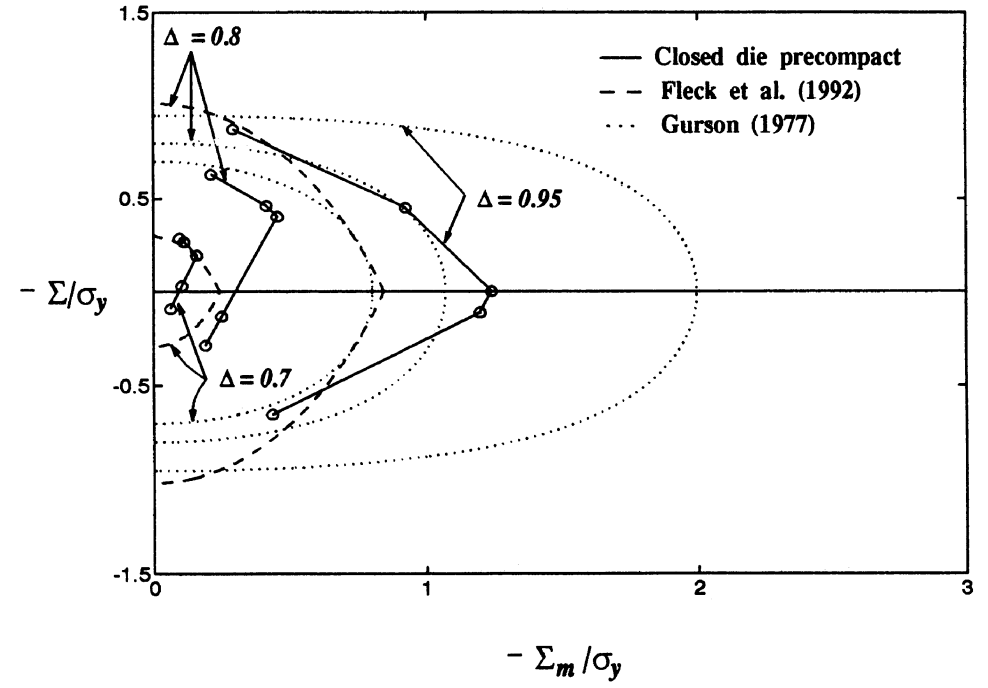

(b)

Fig. 16. Calculated yield surfaces for (a) isostatic precompact, and (b) closed die precompact, compared with the yield criteria of Fleck *et al.* [2] and Gurson [12].

Acknowledgements—The authors are grateful for financial support from the ARPA Contract No. 0014-91-J-4089 through a collaborative programme with the University of Virginia, and for helpful discussions with Dr A. C. F. Cocks.

REFERENCES

1. A. S. Helle, K. E. Easterling and M. F. Ashby, *Acta metall.* **33,** 2163 (1985).
2. N. A. Fleck, L. T. Kuhn and R. M. McMeeking. *J. Mech. Phys. Solids* **40,** 1139 (1992).
3. A. P. Green, *J. Mech. Phys. Solids* **2,** 197 (1954).
4. H. A. Kuhn and C. L. Downey, *Int. J. Powder Metall.* **7,** 15 (1971).
5. K. T. Kim, J. Suh and Y. S. Kwon, *Powder Metall.* **33,** 321 (1990).
6. A. L. Gurson and T. J. McCabe, in *Proc. MPIF/APMI World Congress on Powder Metallurgy and Particulate Materials*, San Francisco, Calif. (1992).
7. S. B. Brown and G. Abou-Chedid, *J. Mech. Phys. Solids* **42,** 383 (1994).
8. A. M. Laptev and A. N. Ul'yanov, *Soviet Powder Metall. Metal Ceram.*, p. 183 (1984).
9. R. Hill, in *The Mathematical Theory of Plasticity*. Oxford University Press, Oxford (1950).
10. A. M. Laptev and S. V. Podlesnyi, *Soviet Powder Metall. Metal Ceram.* **24,** 888 (1985).
11. H. F. Fischmeister and E. Artz, *Powder Metall.* **26,** 82 (1983).
12. A. L. Gurson, *J. Engng Mater. Technol.* **99,** 2 (1977).